

Article

Mineralogy and a New Fertility Index of Alunite in the Fanshan Lithocap, Luzong Basin, Anhui Province, China

Xuanxuan Li ^{1,2,*}, Qingling Xiao ³, Xin Lin ^{1,2}, Shuangfei Li ⁴ and Mingying Tang ⁴¹ Key Laboratory for Mechanics, Anhui Polytechnic University, Wuhu 241000, China; linxin@ahpu.edu.cn² Engineering Research Center of Anhui Green Building and Digital Construction, Anhui Polytechnic University, Wuhu 241000, China³ School of Earth Sciences, Hebei GEO University, Shijiazhuang 050031, China⁴ No. 8 Institute of Geology and Mineral Resources Exploration of Shandong Province, Rizhao 276826, China

* Correspondence: lixuanxuan@ahpu.edu.cn

Abstract: Alunite is used as a representative mineral for indicating deposits in lithocaps, and lithocaps are generally related to the porphyry–(high-sulfidation) epithermal mineralization system. The study of alunite is of theoretical and exploration significance for prospecting potential underlying porphyry and epithermal deposits. Studies on alunite geochemistry have made breakthroughs, but there is little research on alunite mineralogy, for example, using scanning electron microscopy (SEM) images, differential thermal analysis (DTA), and Fourier-transform infrared spectroscopy (FT-IR). This study mainly focuses on alunite micromorphological characteristics, weight loss changes with temperature, and ionic group structure, aiming to identify the relationship between these features and indications for prospecting. The Fanshan lithocap is located in the northwest part of the Luzong basin, Anhui province of China, and it can potentially be used for exploring porphyry and epithermal deposits. Fanshan alunite is formed in two stages with three types of alunite. IA alunite is formed in the early hydrothermal stage and replaces felsic minerals in the Zhuanqiao Formation, IB alunite is formed in the later hydrothermal stage and fills in open spaces with bladed particles, and II alunite is the product of pyrite oxidation and reaction with other minerals in the supergene stage. Alunite electron microprobe data and energy-dispersive spectroscopy data further confirm temperature decreases with hydrothermal evolution, and the presence of a high-sulfidation epithermal system in the Luzong basin. Aside from the forming environment, SWIR, and geochemistry of alunite, there are other indication indexes; for example, the larger peak values at 3480 cm^{-1} and smaller peak values at 1080 cm^{-1} in FT-IR spectra and the deeper exothermic valleys at 750 °C and steeper weight loss slopes in the DTA curve suggest a favorable formation environment for alunite and provide valuable indications for deposit exploration and assessments of mineralization potential.

Keywords: alunite; lithocap; FT-IR; DTA; prospecting

Citation: Li, X.; Xiao, Q.; Lin, X.; Li, S.; Tang, M. Mineralogy and a New Fertility Index of Alunite in the Fanshan Lithocap, Luzong Basin, Anhui Province, China. *Minerals* **2024**, *14*, 395. <https://doi.org/10.3390/min14040395>

Received: 1 March 2024

Revised: 26 March 2024

Accepted: 8 April 2024

Published: 11 April 2024



Copyright: © 2024 by the authors. Licensee MDPI, Basel, Switzerland. This article is an open access article distributed under the terms and conditions of the Creative Commons Attribution (CC BY) license (<https://creativecommons.org/licenses/by/4.0/>).

1. Introduction

Lithocaps are generally a direct manifestation of porphyry–epithermal hydrothermal mineralization systems near the surface, with high-sulfidation epithermal deposits often developed at their roots and the possibility of intrusive bodies hosting porphyry copper–gold deposits at depth [1,2]. The study of lithocaps plays an important economic role in the search for copper, gold, and silver deposits at depth. Alunite is a representative mineral in lithocaps, serving as a direct indicator for deposit exploration [2–4]. Moreover, alunite in different genetic environments exhibits significant differences in guiding deposit exploration [3]. The structure and compositional characteristics of alunite can be used as evidence for recording magmatic–hydrothermal fluid evolution [2–5]. Previous studies have mainly focused on the combination of whole-rock geochemistry, short-wave infrared spectroscopy (SWIR) characteristics of alunite (including mineral identification, half-height

width, absorption intensity, absorption depth, and wavelength position at 1480 nm and its spatial variation features), and geochemical anomalies, and have proposed a set of geochemical exploration methods [3], which have been widely applied and validated. However, there is currently very little research on the mineralogy of alunite, especially its mineral properties, such as microstructure and phase characteristics in different environments, as well as its thermal chemical characteristics, such as differential thermal analysis (DTA) and Fourier-transform infrared spectroscopy (FT-IR). There is limited research on the thermal analysis curves of alunite in different environments and how to use these data to guide deposit exploration. Furthermore, it is unclear whether the thermal analysis curves provide indications for deposit exploration. Therefore, it is necessary to analyze the physical properties of alunite to better utilize its mineralogical characteristics for guiding deposit exploration.

The Luzong basin has a wide variety of mineral resources, large reserves, and high grades. Many types of mineralization have been identified, including Fe deposits, S deposits, Cu deposits, Pb-Zn deposits, Ag deposits, alunite deposits, kaolinite deposits, and other deposits, like U deposits. Among them, alunite reserves rank second in the country [6–8]. The basin is rich in alunite deposits, with over 200 large, medium, and small deposits and mining sites scattered throughout [9]. The Fanshan alunite deposit is located in Fanshan Town, Lujiang County, and is the largest alunite deposit in the Luzong basin. The Anhui Geological Bureau's 327th Geological Team conducted systematic exploration of the alunite deposit in the Fanshan mining area from 1953 to 1966, confirming it as a large-scale alunite deposit with an average grade of 40.39%. Units such as the Anhui Geological Bureau's 327th Geological Team and the District Survey Team have conducted geological exploration and deposit evaluation work in the Fanshan mining area, but the research has mostly focused on the exploration of mineral reserves and has not extended to the study of alunite mineral. In previous studies of porphyry deposits and hydrothermal vein-type deposits in the basin by different scholars, little attention was given to the lithocaps represented by alunite. They were only described as a type of alteration in the geological characteristics of the deposits, with sporadic geochemical work conducted [10–13]. In recent years, as lithocaps have become increasingly familiar, researchers have conducted SWIR and geochemical analysis of alunite in the Fanshan area, indicating the potential for finding porphyry–epithermal hydrothermal deposits and identifying potential mineralization directions [4,14–16]. However, there has been no systematic theoretical study on the mineralogy of alunite.

Based on detailed petrographic observations, electron probe microanalysis (EPMA), scanning electron microscopy (SEM) observations, and energy-dispersive spectroscopy (EDS) analysis, this study investigates the mineralogical characteristics of alunite in the Fanshan lithocap. The chemical composition, crystal structure, morphology, and other mineralogical features of alunite are determined. The chemical composition of alunite further confirms the presence of a high-sulfidation epithermal system in the Luzong basin. In addition, thermal chemical characterization of alunite such as DTA and spectral analysis, including FT-IR, are performed. By combining the mineral structure characteristics of alunite, a practical and feasible method for identifying the heat source and deep-seated concealed intrusive bodies associated with lithocaps is proposed. This research has theoretical and exploration significance. This study deepens the research on lithocaps, provides theoretical support for finding new exploration indicators in lithocaps, and provides important information for deep prospecting. The results of this study have extensive significance for prospecting indicators of porphyry deposits. These new indexes provide further exploration direction for deep deposit prospecting in lithocaps, and promote the work of searching for new exploration indexes.

2. Geology of Luzong Basin

The middle-lower Yangtze metallogenic belt (MLYB) is located in eastern China and has significant mineral potential, hosting iron oxide–apatite (IOA) deposits and porphyry–skarn copper–iron polymetallic deposits [17]. The Luzong basin, situated between Lujiang

County (Lu) and Zongyang County (Zong), is an important polymetallic ore cluster within the MLYB [18,19]. The distribution of the Luzong basin is controlled by three sets of major faults (Figure 1), with the Tancheng–Lujiang Fault to the west, located near the collision zone of the North China and Yangtze plates. The basin has a shallow eastern and deep western basement and is considered an inherited Mesozoic continental basin [20]. The exposed volcanic rocks cover an area of approximately 800 km². The exposed sedimentary strata mainly consist of continental clastic sediments of the Middle Jurassic Luoling Formation (J₂l), which is unconformably overlain by the volcanic rocks. During the Mesozoic Yanshanian period, extensive olivine gabbro assemblages were formed. The volcanic rocks can be divided, from old to young, into the Longmenyuan Formation, Zhuanqiao Formation, Shuangmiao Formation, and Fushan Formation. They exhibit a roughly concentric spatial distribution, with older volcanic rocks distributed closer to the basin’s margins and younger volcanic rocks towards the center (Figure 1). The Longmenyuan Formation is mainly distributed at the basin’s edge, characterized by diorite trachyandesite. The Zhuanqiao Formation is predominantly located in the central part of the volcanic basin, characterized by pyroxene trachyandesite, and constitutes the main body of volcanic rocks in the basin. The Shuangmiao Formation is mainly distributed in the central and southern parts of the basin, characterized by trachybasalt. The Fushan Formation is sporadically distributed in the central part of the basin, with a smaller outcrop area, primarily composed of trachytic volcanic rocks [10,21]. There are unconformable contacts between each formation, forming four cycles [10,20]. The volcanic activity of each cycle starts with explosive eruptions, followed by increasing effusive eruptions, and finally ends with volcanic sedimentation. The eruption style evolves from fissure–central to typical central eruption, and the volcanic rocks consist of lava, clastic lava, pyroclastic rocks, and subvolcanic rocks [10].

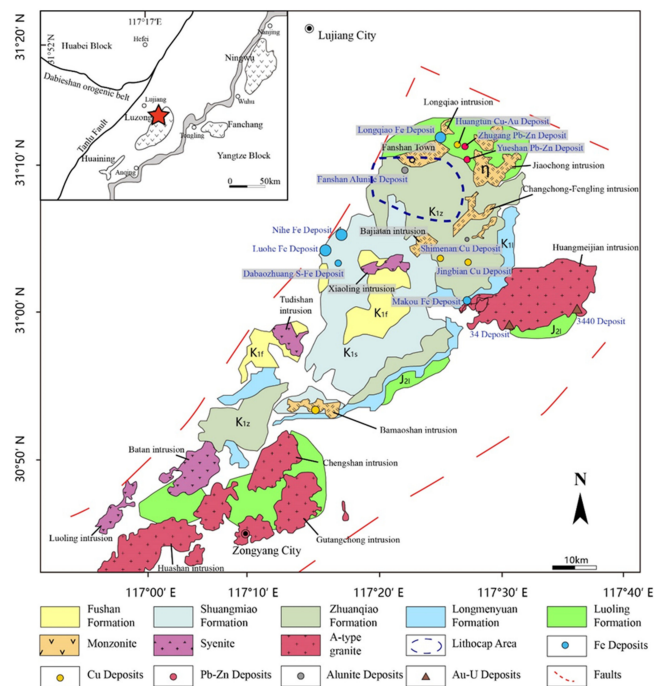


Figure 1. Geology and deposit distribution map of the Luzong basin [22].

There are more than 30 intrusive rock bodies distributed within the Luzong basin [23–26]. The formation of these intrusions is closely related to regional volcanic activity. Based on their lithology, the intrusion can be primarily classified into three types: monzonite, syenite, and A-type granite. Monzonites have a larger outcrop area and were formed during the period of 134–130 Ma. They are mainly distributed in the northern part of the basin and are closely related to the magmatic activity of the Longmenyuan and Zhuanqiao cycles of volcanic rocks, representing different forms of the same magmatic activity. Examples of monzonite bodies

include Bajiatan, Longqiao, and Luoling bodies. Syenites, with a larger outcrop area, were formed during 129–123 Ma and are distributed in the southern part of the basin. They are mainly controlled by volcanic structures and north–northeast trending faults within the basin, corresponding to the magmatic activity of the Shuangmiao and Fushan cycles of volcanic rocks. Examples of syenite bodies include Tudishan and Fenghuangshan bodies. A-type granites are mainly distributed in the southern and southeastern parts of the basin and are primarily controlled by regional north–northeast trending major faults, independent of the basin’s volcanic structures. Examples of A-type granite bodies include Chengshan, Huashan, and Huangmeijian bodies [22,27–29].

The Luzong basin is a mineral cluster consisting of various deposits such as iron, sulfur, copper, lead–zinc, alunite, gold, and uranium. On the western side of the basin, there is Shaxi porphyry Cu (Au) deposit. The main types of deposits within the basin include an Au–Cu deposit-bearing tourmaline breccia pipe (Huangtun deposit, [30]), which is not found in causative intrusions; skarn Fe deposit (Longqiao deposit, [31,32]), iron oxide–apatite deposit (Nihe, Luohe, Dabaozhuang, Makou deposit, [11,33–37]); hydrothermal vein Cu deposit (Jingbian, Shimeinan, [38]); the abovementioned kinds of deposits are related to the Zhuanqiao Formation; Pb–Zn (–Ag) deposits (Yueshan, Zhugang, [39,40]), which are spatially and temporally related to monzonite and diorite intrusions [22,29]; U–Au deposits (34, 3440), which are in time and space related to syenite and A-type granite in the basin margin, respectively [22,41].

In addition to the metallic deposits mentioned above, the basin also has developed nonmetallic mineral deposits, including alunite, gypsum, purple clay (a mixture of kaolinite, quartz, and mica, with a high content of iron oxide), limestone, and kaolinite. The large Fanshan alunite deposit constitutes the center of the Fanshan lithocap in the basin (Figure 2), with a total area of approximately 30 km². The iron ore reserves in the basin exceed 1.2 billion tons, with an average grade of 43.9% [32]. The S–Fe reserves amount to 670 million tons, and the copper metal reserves are 16.61 million tons, including a resource estimate of 15.1147 million tons of gold–copper ore from the Huangtun copper–gold deposit by the Anhui Geological Bureau’s 327th Geological Team in 2017 [42]. The reserves of alunite are 73.18 million tons. The basin has a rich variety of mineralization types and enormous resource reserves, giving it excellent exploration prospects.

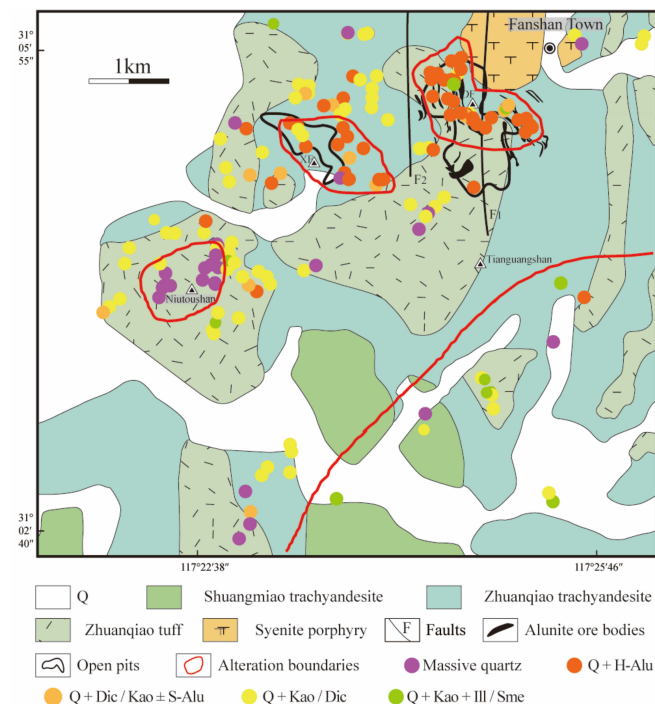


Figure 2. Geological schematic map of Fanshan area [4]. Abbreviations: DF—Dafanshan; XF—Xiaofanshan; Dic—dickite; H–Alu—hydrothermal alunite; Ill—illite; Kao—kaolinite; Q—quartz; S–Alu—supergene alunite; Sme—smectite.

3. Geology of Fanshan Alunite Deposit

The Fanshan alunite deposit is located in the northwest part of the basin and is situated approximately 10 km northeast of the Longqiao Fe deposit and 20 km southwest of the Nihe Fe deposit. The exposed rocks in this area mainly consist of the Lower Cretaceous Zhuanqiao Formation (K_{1z}) and the Shuangmiao Formation (K_{1s}) volcanic rocks (Figure 2). The Zhuanqiao Formation volcanics form the main part of the stratigraphy in the area and are distributed throughout the region. This volcanic unit can be divided into upper and lower sections, which are interbedded and exhibit significant variations in thickness. The lower section is predominantly composed of tuff, with upward transitions into brown-gray almond-shaped porphyritic trachyandesite, purple tuff, tuffaceous siltstone, and breccia tuff. It is in unconformable contact with the underlying Longmenyuan Formation due to volcanic eruption. The rocks in this section undergo alunite and kaolinite alteration, and disseminated pyrite is observed in the deeper parts of the drill holes, occurring in a star-like pattern. The upper section is dominated by trachyandesite, with several layers of purple-red tuffaceous siltstone intercalated. It is in parallel unconformable contact with the underlying tuff. This section exhibits varying degrees of alunite alteration, kaolinite alteration, and silicification. The Shuangmiao Formation volcanic rocks are exposed in the southwestern part of the mining area, overlying different levels of the Zhuanqiao Formation in an unconformable manner. This formation can be divided into upper and lower sections, with tuff and trachyandesite as the dominant lithologies.

The volcanic structures in the Luzong basin can be divided into primary structures and secondary structures. The primary structures form a large-scale volcanic depression that constitutes the entire volcanic rock basin. They are mainly controlled by the Tan-Lu deep fault in the western part. The secondary structures are secondary volcanic structures controlled by various fault structures within the basin [43]. The Fanshan alunite deposit is mainly located in the caldera of the Zhuanqiao eruption phase. The area forms a large volcanic depression with a ring-shaped structure, which is a component of the Luzong basin volcanic primary volcanic structure [43,44]. The frequent activity of ring-shaped fault fissure structures and the well-developed small-scale fault fissure structures in the peripheral areas of the caldera provide space for the migration of hydrothermal fluids. The significant faults in the area include the Dafanshan normal fault (F_1) and the Xishan normal fault (F_2) (Figure 2), which cut through the Fanshan alunite orebodies and volcanic rocks in a north–south direction, and they are post-mineralization structures. Folding structures are not well developed in the volcanic rock series of the mining area, which mainly consists of monoclinical structures composed of Zhuanqiao Formation volcanic lavas and volcanic clastic rocks. The strike of the volcanic rocks is approximately 140° , dipping to the southwest at an angle of 25° to 40° . The orientation of some formations may slightly vary due to the influence of intrusive bodies. The intrusions in the area are mainly composed of syenite, occurring as small intrusions and dikes primarily in the northwestern part of the mining area. They have a disruptive effect on the Fanshan alunite orebodies and volcanic rocks. These intrusive rocks are post mineralization and formed later than the Fanshan alunite deposit, causing the destruction of the lithocap [15] (Figure 2).

The alunite orebody is primarily formed by the alunite mineralization of the Zhuanqiao Formation trachyandesite and tuff. The areas with higher alunite content are considered to be the orebodies. The boundary between the orebody and the surrounding rocks is not distinct, showing a gradual transitional relationship. The orebodies mainly occur as layer-like, lens-like, and irregular shapes, following the bedding or occurring along the fractures between tuff and trachyandesite layers, with a dip angle of 25° to 40° . The thickness of the orebodies varies from a few meters to 60 m, with the maximum thickness reaching 110 m. The length of the orebodies ranges from 150 to 950 m, and the inclination depth is between 100 and 400 m. The average grade of the alunite orebody is 32.5% to 39%, with some sections

having an average grade exceeding 45%. The main occurrence is within the tuff, while the lower-grade orebodies with an average grade of 20% to 35% are mostly found within the trachyandesite [9]. The ore exhibits a fine-grained texture and porphyritic-like texture, with disseminated deposits being predominant. The alunite mainly occurs in a fine-grained form, with some foliation. The main ore mineral is alunite, and associated gangue minerals include quartz, kaolinite, and dickite, with minor amounts of illite, pyrophyllite, nacrite, illite–smectite, and limonite, while pyrite is absent or present in trace amounts. The main alterations include silicification, kaolinite alteration, dickite alteration, pyrophyllite alteration, minor chlorite alteration, and hematite.

4. Mineralization and Alteration

4.1. Alterations

The Fanshan lithocap is primarily formed by the intense alteration of the Zhuanqiao Formation trachyandesite and tuff. The main mineralization is alunite, and the alterations include silicification, kaolinite, dickite, muscovite, pyrophyllite, pyrite, goethite, and illite–smectite [14]. Silicification is mainly represented by vuggy quartz and massive cryptocrystalline quartz. Vuggy quartz is formed by leaching of acidic fluids on the trachyandesite or volcanoclastics and is mainly distributed in the trachyandesite of the Dafanshan mining area, with some quartz cavities filled with alunite (Figure 3a). In the Niutoushan area, due to the control of tuff lithology, quartz occurs as dense massive forms. In the area to the southeast of the mining area, a small amount of low-temperature silica alteration can be observed (Figure 3f). Alunite, in a light-red color, is widely distributed in the matrix of the surrounding rocks or replaces plagioclase phenocrysts (Figure 3b), with a higher content in the Dafanshan and Xiaofanshan mining areas. Pyrite occurs mainly as fine-grained crystals associated with alunite in the Dadanshan mining area, and most of the pyrite has been oxidized to hematite. In the Dafanshan mining area, a small amount of pyrophyllite can be observed filling fractures (Figure 3e). Kaolinite and dickite mainly occur as extensive alterations, and both minerals replace feldspar phenocrysts and feldspathic minerals in the matrix, retaining the phenocrystic crystal form (Figure 3c). Dickite also occurs separately as aggregates replacing feldspar phenocrysts or as vein-like occurrences (Figure 3d). Illite–smectite mainly results from the alteration of feldspar and muscovite in the trachyandesite.

The alteration exhibits zonation in space based on the occurrence of these minerals. From the Dafanshan alunite deposits to the southwest Niutoushan area and further south, the sequence of vuggy quartz–hypogene alunite–pyrite, quartz–kaolinite–dickite–supergene alunite, and kaolinite–illite–smectite are developed. In the Niutoushan area, residual massive quartz develops (Figure 2, [4,15]). The Fanshan lithocap exhibits hilly landforms at higher elevations in the Dafanshan, Xiaofanshan, and Niutoushan areas because of the presence of quartz and alunite. The surface oxidation of iron-bearing minerals gives a reddish-brown color to the exposed outcrops. The areas around the Xiaofanshan and Niutoushan show stronger alteration of kaolinite and dickite, which have undergone erosion and have lower elevations, with significant vegetation cover.

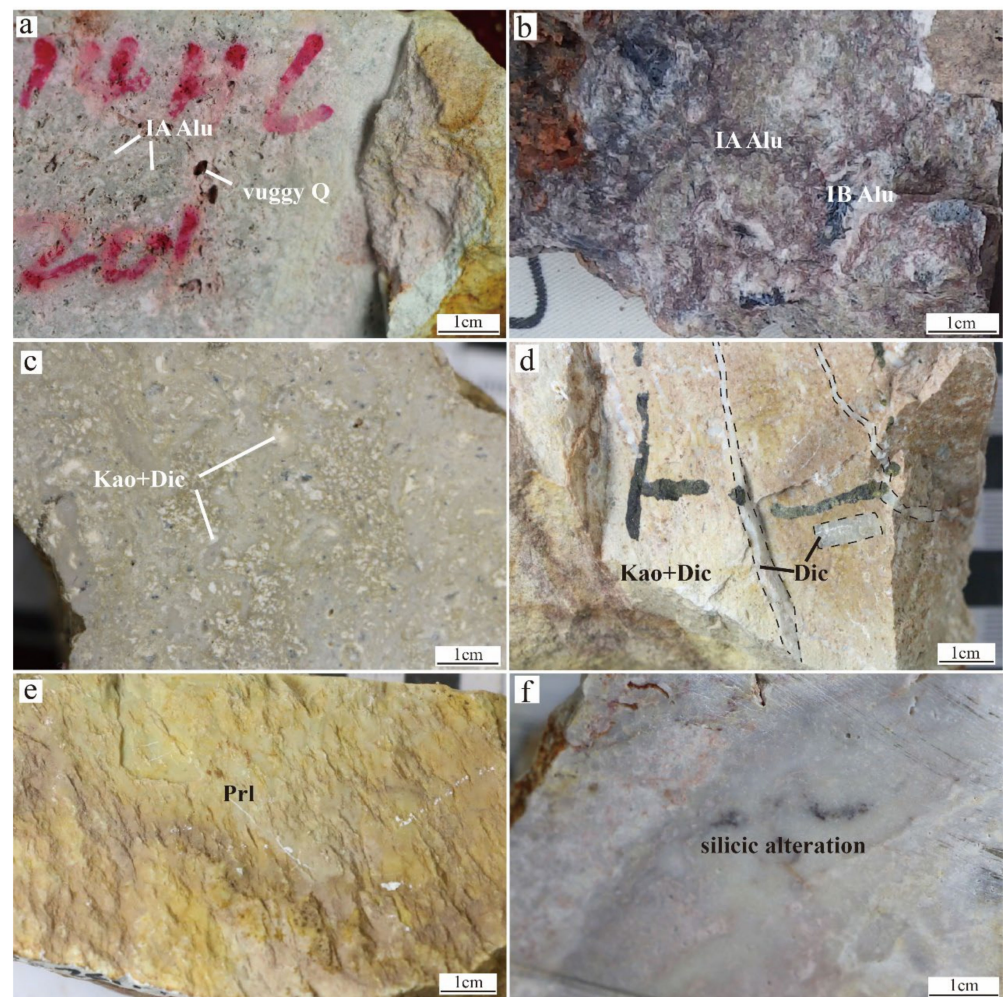


Figure 3. Characteristics of altered minerals of the Fanshan lithocap in the Luzong basin [15]. (a) The feldspar minerals in the original trachyandesite or pyroclastic rocks are leached and leave pores to form vuggy quartz, and the matrix is filled with quartz and alunite; (b) foliated alunite aggregates are filled in open space, mainly in quartz porous media; (c) trachyandesite in which feldspar phenocrysts are replaced by kaolinite and dickite, the white minerals of different sizes are kaolinite and dickite that have replaced feldspar phenocrysts, feldspar minerals in matrix are mostly altered; (d) well-crystallized dickite aggregates preserve the crystal structures of feldspar phenocrysts, earlier kaolinite and dickite alterations are cut by later dickite veins; (e) pyrophyllite alteration as extensive distributions along the fissure surface, this image shows the fissure surface, and the yellowish-green or brown mineral is pyrophyllite; (f) silica alteration formed at low temperature is mainly composed of silica. Abbreviations: IA-Alu—hydrothermal early-stage alunite; IB-Alu—hydrothermal later stage alunite; vuggy Q—vuggy quartz; Kao—kaolinite; Dic—dickite; Prl—pyrophyllite.

4.2. Alteration and Mineralization

The formation of altered minerals in the Fanshan lithocap is divided into hydrothermal and supergene stages (Figure 4, [15]). The volcanic rocks of the Zhuanqiao Formation undergo various types of alteration during the hydrothermal stage. In the early stage, vuggy quartz, alunite, pyrite, pyrophyllite, and a small amount of well-crystallized kaolinite and dickite are formed. Tuff mainly undergoes alunite alteration (and aluminum–phosphate–sulfite, APS), silicification, and weak pyrophyllite alteration. Trachyandesite exhibits weaker alunite alteration, primarily developing clay alteration, including kaolinite, dickite, and minor illite. In the late stage, alunite is mainly developed, and, compared to the early stage, kaolinite and dickite further develop as widespread alterations. The two types of alunite during the hydrothermal stage are related to the hydrothermal ore-forming

fluids in the area [4]. During the supergene oxidation stage, hematite and limonite are evident, and jarosite and low-temperature alunite appear. Feldspar minerals are altered into illite–smectite minerals under this low temperature and oxidation at the surface.

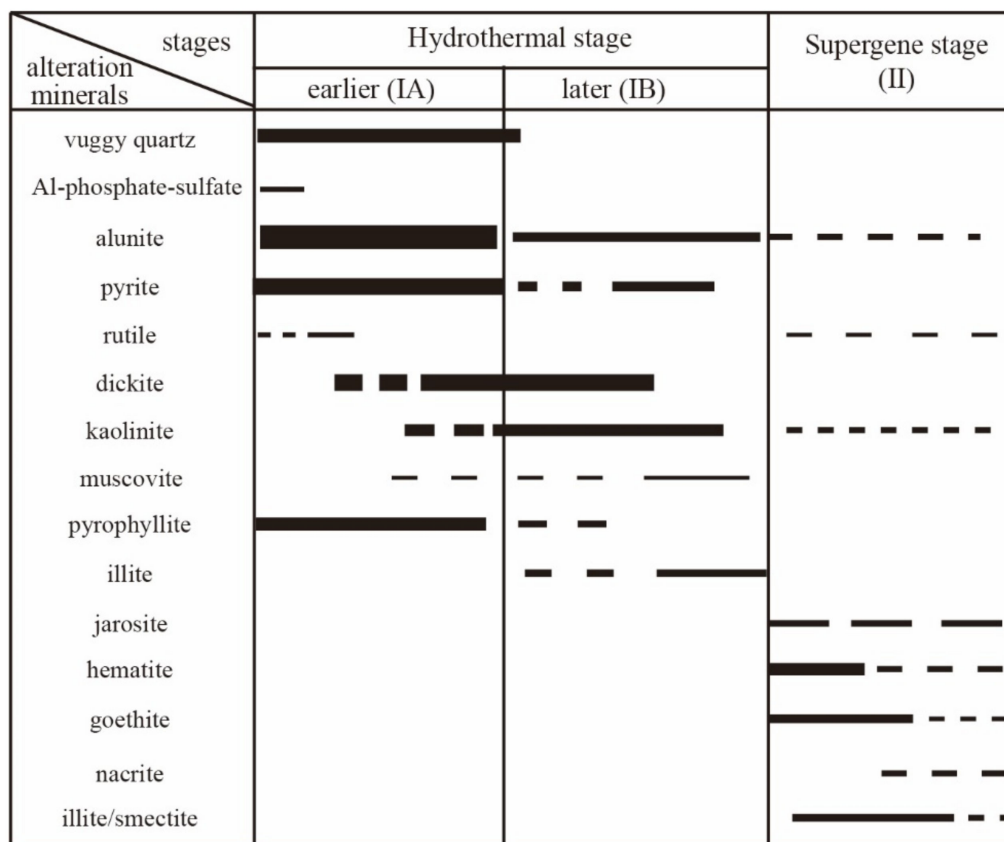


Figure 4. The formation stages of mineralization and alteration in the Fanshan lithocap, Luzong basin [15].

5. Analysis Methods and Samples

The alunite samples used in this experiment were mainly collected from the Fanshan alunite mining area. Petrographic observations and electron probe microanalysis (EPMA) were conducted on alunite samples of different origins. Additionally, scanning electron microscopy–energy-dispersive spectroscopy (SEM-EDS) and thermal analysis techniques such as differential thermal analysis (DTA) and Fourier-transform infrared spectroscopy (FT-IR) were performed. However, due to the small particle size of most alunite samples, which typically falls below the analysis requirement of 30 μm to 40 μm for EPMA, the analysis scope was limited. Therefore, larger crystals of alunite from the hydrothermal stage and a few samples from the supergene stage were primarily selected for EPMA. SEM-EDS was used to observe the microscopic morphological characteristics of the alunite and analyze variations in element composition.

The alunite samples were prepared as probe mounts with a thickness of approximately 0.02 mm for microscopic observation. Representative alunite samples with larger crystals were then selected for EPMA. The EPMA was conducted at the Electron Probe Laboratory of the School of Resources and Environmental Engineering, Hefei University of Technology. The analysis was performed using a JEOL JXA-8230 instrument (JEOL Ltd., Tokyo, Japan) with an accelerating voltage of 15 kV, a beam current of 10–20 nA, and a spot size of 3–5 μm. The analysis employed 53 mineral standards from SPI Corporation in New York, United States. Matrix effects were corrected using the PRZ method, and the accuracy of the element analysis ranged from 1% to 5%.

The samples need to be prepared as blocks measuring 5 mm * 5 mm in size prior to the SEM and EDS experiments. The sample surfaces are coated with a gold spray to enhance their conductivity. Subsequently, the prepared samples are placed in the sample chamber for scanning electron microscopy and energy-dispersive spectroscopy analysis. These experiments were conducted at the Analysis and Testing Center of Hefei University of Technology. The instrument used was the JSM-6490LV (JEOL Ltd., Tokyo, Japan) from Japan, with the following main performance parameters: a point resolution of 3 nm under tungsten filament illumination, an acceleration voltage range of 0.5–30 kV, and a magnification range from 5* to 300,000*. The X-ray energy-dispersive spectrometer system used a Si (Li) detector with an energy resolution of 133 eV. It can analyze elements from 5B to 92U, with a spectral acquisition time of 50 s and a spectral acquisition area of a 12 μm * 12 μm square.

The differential thermal analysis (DTA) experiment was conducted at the Analysis and Testing Center of Hefei University of Technology using a STA449F3 instrument made by Netzsch Group, Hanau, Germany. The temperature range of the instrument is 25 to 1450 °C, with a heating rate of 10 °C/min.

For the Fourier-transform infrared spectroscopy (FT-IR) analysis, representative alunite samples were selected for infrared spectral testing. This experiment was also carried out at the Analysis and Testing Center of Hefei University of Technology. The instrument used was a Nicolet 6700 Fourier-transform infrared spectrometer made by Manufacturer of Thermo Fisher Scientific Inc, Waltham, Massachusetts, USA). The spectral range of the instrument is 400 cm^{-1} to 12,000 cm^{-1} , with a resolution of 0.09 cm^{-1} and a linearity of $\leq 0.07\%$.

The selected sample numbers for the experiment are FS14XX407, FS14HL204, FS14XX411, FS14LZ004, FS14HL202, and FS14YN058. The degree of crystallization of alunite decreases in the following order. The alunite in sample FS14XX407 was formed in the late stage of hydrothermal activity (IB alunite) and is of hypogene origin. The alunite in samples FS14HL204, FS14XX411, FS14LZ004, and FS14HL202 was formed in the early stage of hydrothermal activity (IA alunite) and is also of hypogene origin. The alunite in sample FS14YN058 is a product of supergene activity (II alunite) and is of supergene origin. When conducting geochemistry analysis of alunite, we mainly selected K-Na series alunite with relatively uniform and zoneless composition in BSE images to avoid the influence of the results caused by composition zonation.

6. Alunite Mineralogy and Geochemistry

6.1. Alunite Mineralogy and Microstructure

There are significant differences in alunite occurrence in Fanshan, and alunite is present in both the early and late stages of hydrothermal activity, as well as during the supergene period. Alunite can be classified into three types based on the formation time and texture characteristics. SEM analysis is conducted on alunite samples of different origins to observe their microscopic features. This analysis plays a crucial role in prospecting by direct indication of alunite texture.

The early-stage hydrothermal alunite (IA) is produced through metasomatism of the surrounding rocks by hydrothermal fluids. It mainly exhibits metasomatic alteration and has a widespread distribution (Figure 5a,c). It is widely distributed in open-pit mines and deep underground orebodies in the Dafanshan mining area. The alunite formed from feldspar phenocrysts and matrix in hydrothermal-altered trachyandesite mainly coexists with quartz and pyrite. This alunite has a subhedral to anhedral texture, with grain sizes ranging from 0.2 mm to 1 mm. It is densely disseminated throughout the rock (Figure 5a,b). Alunite found in tuff mainly coexists with quartz, exhibiting a subhedral, equigranular texture (Figure 5d) and a densely disseminated distribution (Figure 5c). The micromorphological features of IA alunite primarily include plate-like and variably sized grains (Figure 6b–e), with a few grains showing aluminum–phosphate–sulfate (APS) mineral inclusions (Figure 5h).

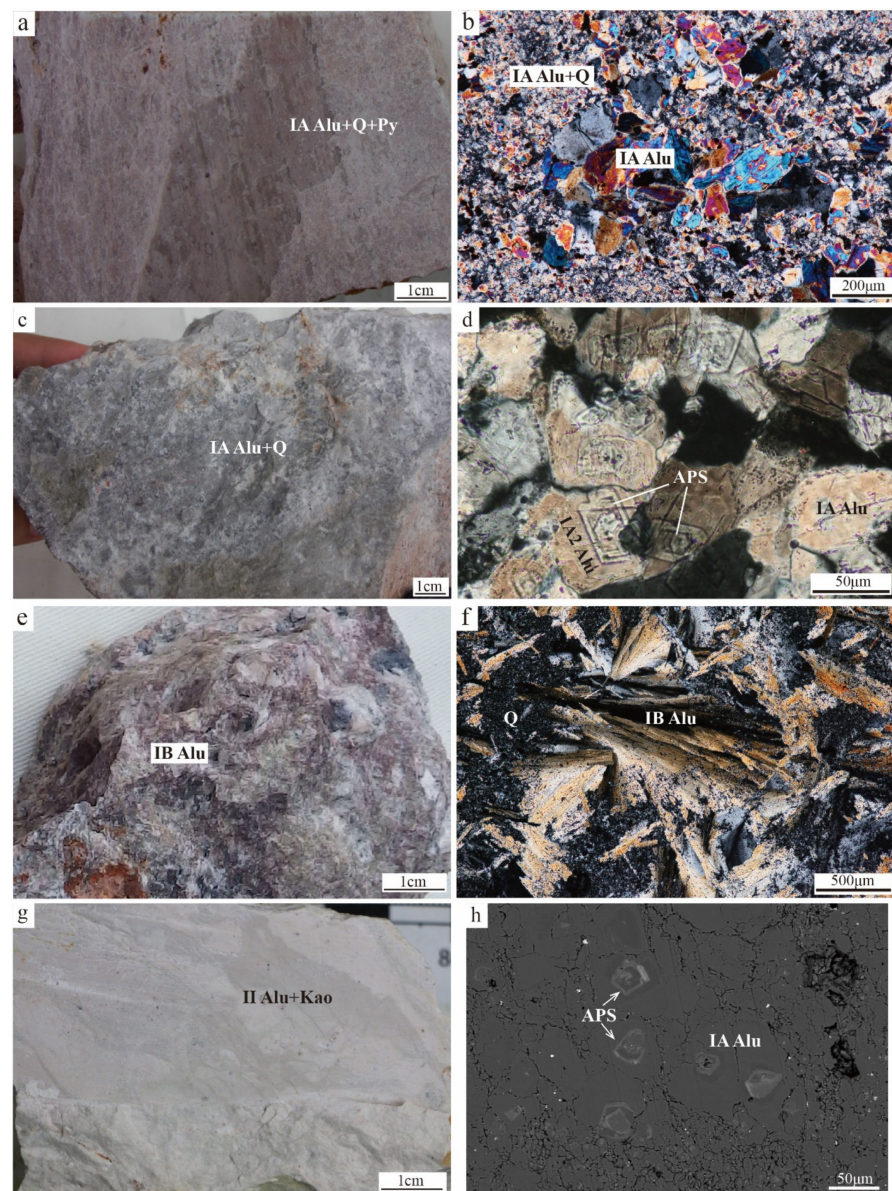


Figure 5. Characteristics of alunite in Fanshan lithocap, Luzong basin. (a) Photo of purplish-red dense alunite formed in the hydrothermal stage [4]; the original rock was Zhuanqiao trachyandesite, and the texture was destroyed by intense alunite alteration. The IA alunite coexists with minor pyrite; (b) photomicrograph of subhedral equigranular IA alunite in Zhuanqiao trachyandesite pervasively replacing felsic minerals; granular alunite retains the form of the phenocrysts, and there is mainly quartz and minor fine-grained alunite in the groundmass (cross-polarized light); (c) photo of gray dense alunite formed in the hydrothermal stage [4]. The original rock is Zhuanqiao tuff, and the IA alunite coexists with quartz; (d) photomicrograph of IA alunite exhibiting extensive and uniform alterations in Zhuanqiao tuff. The IA alunite is subhedral, equigranular, densely disseminated, and cemented by quartz, and APS minerals are developed in the cores of the alunite crystals (cross-polarized light) [16]; (e) photograph of translucent bladed alunite formed in the hydrothermal stage; IB alunite fills the open spaces; (f) photomicrograph of coarse-grained IB alunite with strong cleavage filling in quartz pores; fractures are filled with minor rutile and hematite (cross-polarized light); (g) photograph of white to pinkish powdery II alunite coexisting with kaolinite in the supergene stage [4]. (h) SEM-BSE image of APS minerals in cores of IA alunite; the light color is mainly due to Svanbergite. Abbreviations: Alu—alunite; APS—aluminum-phosphate-sulfate; Hem—hematite; Kao—kaolinite; Py—pyrite; Q—quartz.

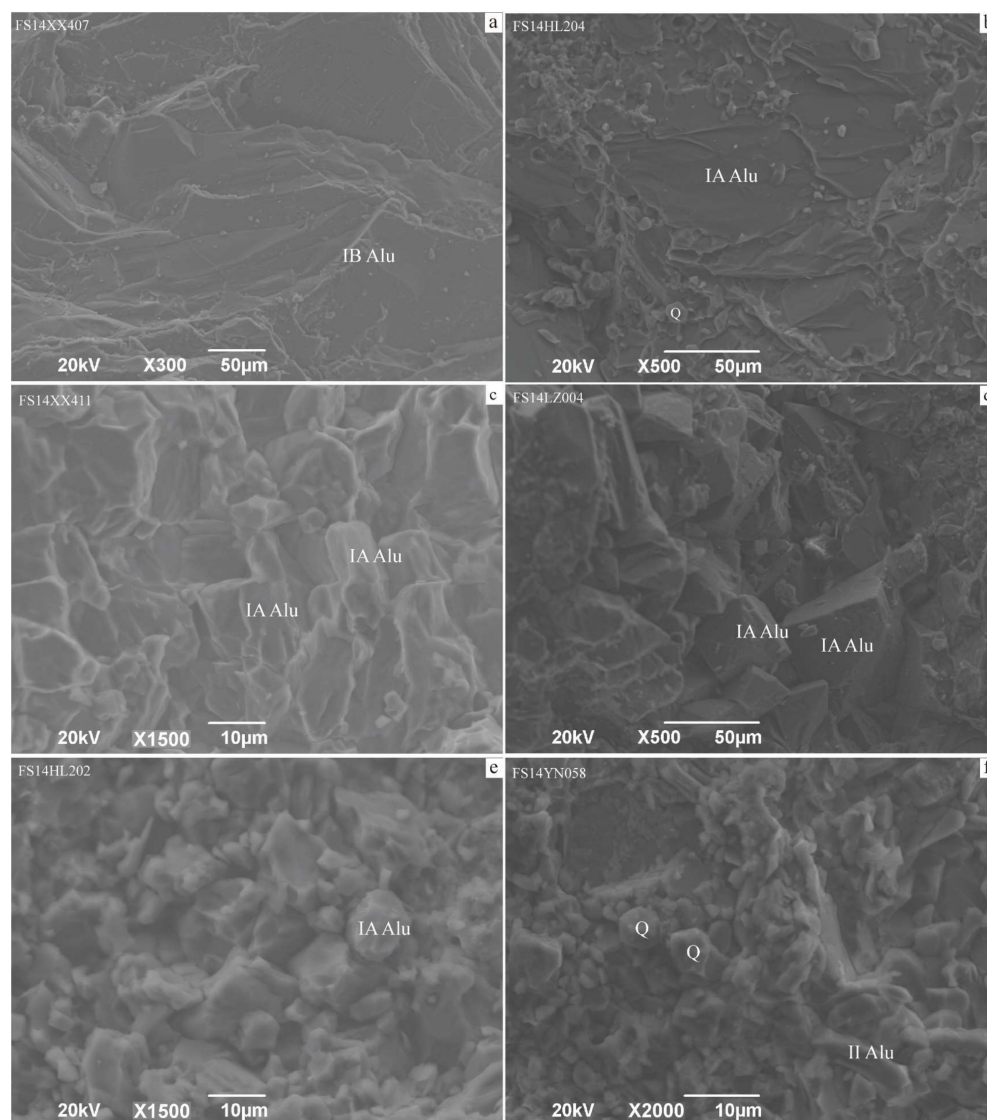


Figure 6. Scanning electron microscope SEM-secondary electron image of Fanshan alunite. (a) The IB alunite filled the pores in the late hydrothermal stage, showing thick blade shape and coarse particles; (b–e) the early metasomatism altered IA alunite, showing plate, subhedral and equigranular particles, with different particle sizes; (f) supergene II alunite, showing irregular thin strips. Abbreviations: Alu—alunite; Q—quartz.

The late-stage hydrothermal alunite (IB) precipitates in open spaces (Figure 5e) and forms after the formation of vuggy quartz. It mainly coexists with quartz, minor hematite, and rutile. The distribution of IB alunite is relatively limited, mainly occurring in the mining pits of the Dafanshan mining area. Its content significantly decreases, but the particle size increases notably, with sizes reaching 5 mm (Figure 5f). It exhibits a densely disseminated distribution in the form of leaf-like aggregates (Figure 5e). The micromorphological features of IB alunite mainly appear as thick plate-like textures (Figure 6a).

Supergene alunite (II) is formed in the latest stage (Figure 4). It is a product of long-term oxidation or weathering of pyrite in lithocaps at or near the surface [16]. It is commonly found on the surface throughout the distribution area of the Fanshan lithocap, albeit in small quantities. It closely associates with quartz, iron oxide minerals, kaolinite, and jarosite. It appears as cryptocrystalline aggregates distributed along fractures. In hand specimens, it appears as soil-like or white powdery aggregates (Figure 5g). The micromorphological features of II alunite exhibit a fibrous appearance (Figure 6f).

6.2. Alunite Geochemistry

The EPMA results of several alunite types are shown in Table 1. The content of alunite varies at different stages and origins. From IA alunite (FS14HL204, FS14XX411, FS14LZ004, FS14HL202) to IB alunite (FS14XX407), and then to II alunite (FS14YN058), the contents of Na₂O, CaO, and H₂O decrease, while the K₂O content increases (Figure 7). The SO₃ content shows little variation (Table 1).

Table 1. Electron probe micro-analysis (EPMA) data (wt%) of Fanshan alunite.

Alunite Types	No. Samples	Al ₂ O ₃	K ₂ O	CaO	Na ₂ O	SO ₃	FeO	Total	H ₂ O	K/Na (mol)
IB	FS14XX407-1	35.05	9.88	0.02	0.56	37.32	0.04	82.93	17.07	19.74
IB	FS14XX407-2	35.25	9.81	0.05	0.72	37.25	0.03	83.15	16.85	15.32
IB	FS14XX407-3	35.34	9.38	0.03	0.86	37.09	0.03	82.76	17.24	12.15
IB	FS14XX407-4	35.22	9.82	0.05	0.46	37.11	0.02	82.68	17.32	23.83
IB	FS14XX407-5	35.04	10.18	0.02	0.41	36.86	0.03	82.54	17.47	27.63
IB	FS14XX407-6	35.01	9.86	0.02	0.39	37.30	0.05	82.65	17.35	28.27
IA	FS14HL204-1	35.56	8.60	0.01	1.38	37.93	-	83.50	16.50	6.98
IA	FS14HL204-2	35.29	8.93	0.01	1.27	36.97	0.01	82.55	17.45	7.90
IA	FS14HL204-3	35.64	9.50	0.02	0.91	37.28	-	83.41	16.59	11.63
IA	FS14HL204-4	35.06	8.21	-	1.49	37.18	-	81.98	18.02	6.18
IA	FS14XX411-1	34.93	10.14	0.02	0.48	36.09	0.04	81.70	18.30	23.49
IA	FS14LZ004-1	35.48	7.30	0.01	0.54	36.25	0.06	79.78	20.22	15.18
IA	FS14LZ004-2	36.13	7.21	0.03	0.61	35.87	0.19	80.10	19.91	13.13
IA	FS14HL202-1	36.82	5.40	0.11	1.43	37.42	0.14	81.46	18.54	4.21
IA	FS14HL202-2	37.13	3.65	0.06	2.38	37.17	0.10	80.67	19.33	1.72
IA	FS14HL202-3	36.49	4.75	0.14	1.65	35.80	-	78.93	21.07	3.22
II	FS14YN058-1	36.87	8.04	0.01	0.46	37.20	-	82.59	17.41	19.58
Theoretical values		36.92	11.37	-	-	38.66	-	-	13.05	-

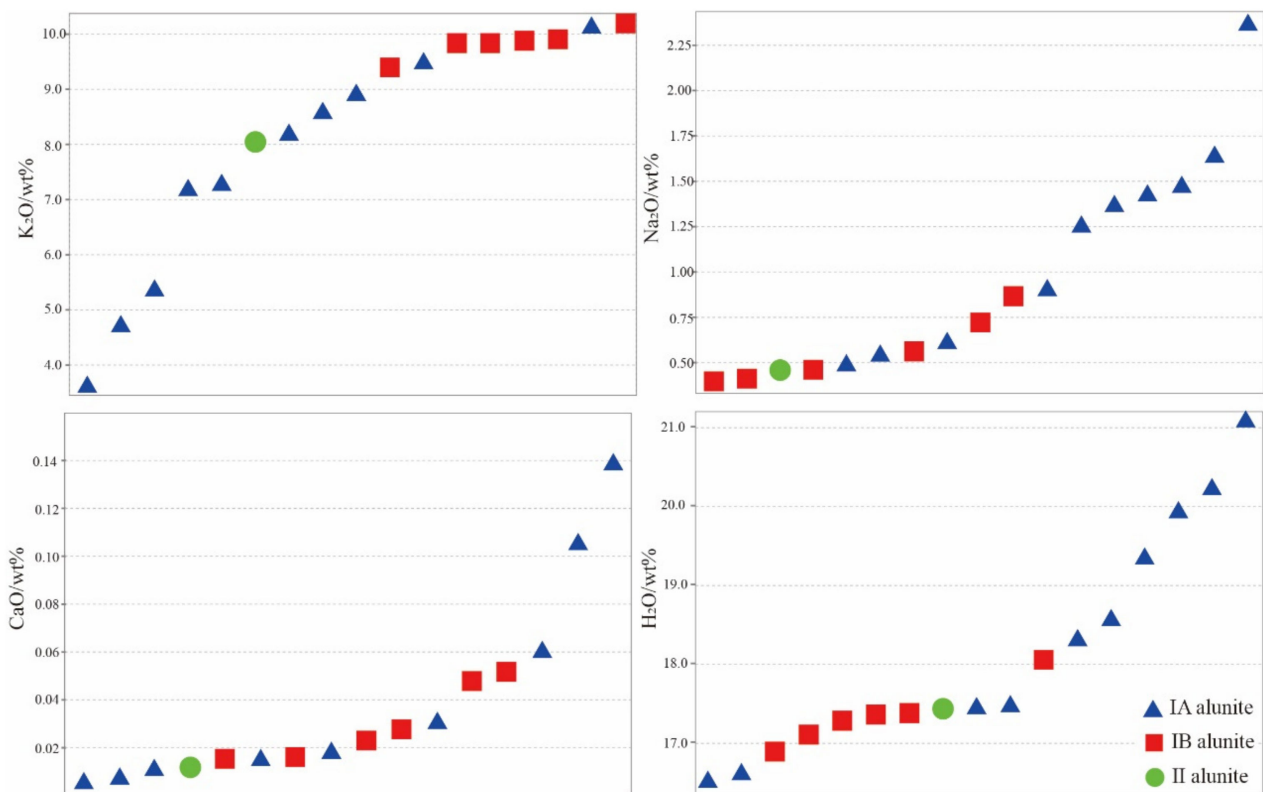


Figure 7. Changes in main element contents in electron probe data of Fanshan alunite.

The theoretical values of K_2O , Al_2O_3 , SO_3 , and H_2O in alunite are 11.37%, 36.92%, 38.66%, and 13.05%, respectively [45]. Compared to the theoretical content, Fanshan alunite contains lower amounts of K_2O and Al_2O_3 , and an excess of H_2O ($\geq 16.59\%$). Additionally, aluminum in alunite can be substituted with iron [46], but after the replacement of the element, the electric price imbalance in the chemical formula requires OH to be converted to H_2O to maintain the charge balance [47]. Therefore, the excess water is used to compensate for the deficiency in the aluminum site, resulting in nonstoichiometric alunite. EPMA results indicate that alunite contains a small amount of Ca (mainly occupying the K site) [46] and Fe (Table 1). Considering the measured SO_3 value is close to the theoretical SO_3 value in alunite, and ignoring the influence of minor elements Ca and Fe, the total chemical formula of alunite in the area is calculated as $(Na_{0.131}K_{0.762})Al_{3.029}(SO_4)_2(OH)_6$ based on the assumption of two SO_4^{2-} ions [47,48], which belong to the K-alunite.

During the SEM observation of alunite samples, EDS analysis was conducted. The results show that the main elements of alunite include S, Al, K, O, and minor Na and F (Table 2). The results of elemental content are shown in Table 2 (H element cannot be measured by EDS analysis for hydrated minerals). The content is expressed as the weight percentage (wt%) of each element. The results contain a certain amount of Si element because of the presence of trace amounts of quartz and clay minerals at the analysis positions. By excluding the testing points with impurities, the O content in relatively pure alunite ranges from 22.28% to 60.77%, with an average of 48.51%; the Al content ranges from 14.17% to 25.76%, with an average of 21.48%; the S content ranges from 13.50% to 36.53%, with an average of 19.65%; the K content ranges from 3.39% to 17.42%, with an average of 8.80%; the Na content ranges from 0.24% to 3.29%, with an average of 1.13%; and the F content ranges from 1.99% to 3.09%, with an average of 2.48%. The overall analysis results indicate that alunite is predominantly K-alunite, consistent with the results of EPMA.

Table 2. Content of elements in SEM-energy-dispersive spectroscopy analysis of alunite (wt%).

Elements	FS14XX407					FS14HL204					FS14XX411									
O	43.94	54.40	44.79	44.50	51.72	47.29	48.75	44.46	50.74	50.23	40.40	29.91	52.01	54.15	60.17					
Al	20.43	18.06	17.78	22.83	21.57	21.45	21.75	22.39	21.02	20.97	23.90	18.85	20.75	20.49	19.17					
Si	5.36	4.24	-	-	0.81	1.07	-	-	-	-	1.35	6.21	0.16	-	-					
S	21.19	15.20	24.79	21.71	16.87	21.02	19.49	22.76	17.76	17.83	22.33	27.39	17.73	16.59	13.77					
K	9.08	6.58	12.18	10.73	7.69	8.53	7.23	8.98	7.19	6.99	10.52	17.48	8.49	8.21	6.28					
Na	-	1.51	0.45	0.24	1.34	0.63	0.79	1.41	0.93	0.90	1.50	0.16	0.86	0.57	0.61					
K/Na (mol)	-	2.57	15.96	26.37	3.38	7.98	5.40	3.76	4.56	4.58	4.14	64.43	5.82	8.49	6.07					
F	-	-	-	-	-	-	1.99	-	2.36	3.09	-	-	-	-	-					
Elements	FS14XX411					FS14LZ004					FS14HL202					FS14YN058				
O	56.80	44.80	60.35	38.31	35.73	50.87	22.28	60.11	57.16	60.77	51.98	57.02	49.78	37.08	37.35					
Al	20.34	21.05	20.51	25.76	24.21	21.70	24.03	14.17	20.60	19.90	21.96	20.31	23.75	24.32	25.15					
Si	-	-	-	-	-	0.02	-	-	-	-	-	-	-	-	-					
S	15.17	21.65	13.60	22.85	26.40	18.65	36.53	14.05	15.51	13.50	18.65	15.99	18.24	22.17	23.27					
K	6.98	11.70	4.61	12.42	14.50	8.76	17.42	4.38	5.07	3.69	4.30	3.39	7.53	16.10	13.79					
Na	0.71	0.80	0.93	0.66	-	-	-	1.91	1.66	2.15	3.11	3.29	0.70	0.33	0.44					
K/Na (mol)	5.80	8.63	2.92	11.10	-	-	-	1.35	1.80	1.01	0.82	0.61	6.34	28.77	18.48					

6.3. Alunite FT-IR Features

The Fourier-transform infrared (FT-IR) absorption spectra of alunite in this region are shown in Figure 8. Sharp absorption peaks appear around 3480 cm^{-1} and 1026 cm^{-1} , a sharp symmetric absorption band appears around 1080 cm^{-1} , and weaker absorption peaks appear around 800 cm^{-1} , 600 cm^{-1} , and 680 cm^{-1} .

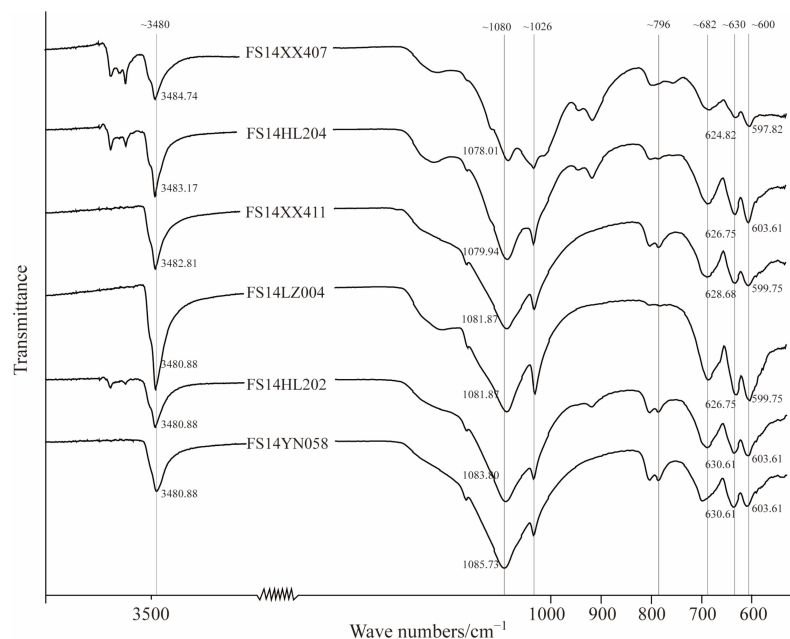


Figure 8. Fourier-transform infrared absorption of Fanshan alunite.

$[SO_4]^{2-}$ is a tetrahedral group with four theoretically possible vibration modes [49]. In FT-IR absorption spectra, it mainly exhibits symmetric stretching vibration mode ν_1 ($900\text{--}1027\text{ cm}^{-1}$), in-plane bending vibration ν_2 ($440\text{--}575\text{ cm}^{-1}$), antisymmetric stretching vibration mode ν_3 ($1050\text{--}1200\text{ cm}^{-1}$), and out-of-plane bending vibration ν_4 ($600\text{--}670\text{ cm}^{-1}$) absorption bands [49]. The strongest is ν_3 , followed by ν_4 , and both show splitting. Clearly, the FT-IR spectrum of alunite in this mine shows a small antisymmetric absorption band near 1220 cm^{-1} , a symmetric absorption band near 1080 cm^{-1} , and weak absorption bands around 600 cm^{-1} and 680 cm^{-1} . These characteristics indicate the presence of tetrahedral $[SO_4]^{2-}$ groups typical of sulfate salts [49]. The ν_3 and ν_4 modes exhibit strong intensity and splitting, while the ν_1 and ν_2 modes are less pronounced. This corresponds to the highest characteristic frequencies of stretching vibration (ν_3) and bending vibration (ν_4) of $[SO_4]^{2-}$ in all XY_4 groups [49].

From hydrothermal alunite (IA and IB, FS14HL204, FS14XX411, FS14LZ004, FS14HL202, FS14XX407) to supergene alunite (II, such as FS14YN058), as shown in the spectral curves from top to bottom (Figure 8), the better the crystallization of alunite, the larger the peak value at 3480 cm^{-1} and the smaller the peak value at 1080 cm^{-1} , showing a clear negative correlation (Figure 9).

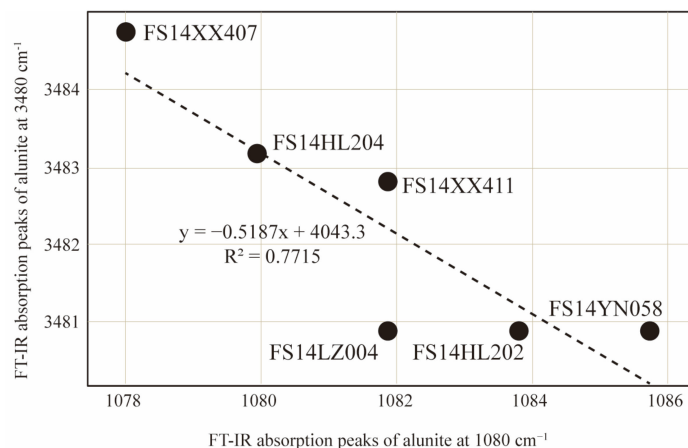


Figure 9. Correlation of Fourier-transform infrared absorption spectra of Fanshan alunite at 3480 cm^{-1} and 1080 cm^{-1} .

6.4. Alunite DTA Results

The differential thermal analysis (DTA) results of alunite show two distinct endothermic reaction stages (Figure 10), and alunite undergoes weight loss during these two endothermic stages. The first endothermic reaction occurs in the range of 540–570 °C, during which alunite transforms into potassium aluminum sulfate ($KAl(SO_4)_2$) and aluminum sulfate ($Al_2(SO_4)_3$). The second endothermic reaction occurs at 760 °C, where potassium aluminum sulfate decomposes, losing SO_2 and forming aluminum oxide (Al_2O_3) and potassium sulfate (K_2SO_4) [47,48]. The depth of the endothermic valleys and the extent of weight loss vary among different stages of alunite. From the early hydrothermal IA alunite (FS14HL204, FS14XX411, FS14LZ004, FS14HL202) to the late hydrothermal IB alunite (FS14XX407), and finally to the supergene II alunite (FS14YN058), both endothermic valleys of alunite show a gradually shallow trend, and the slope of the weight loss curve gradually becomes gentler (Figure 10).

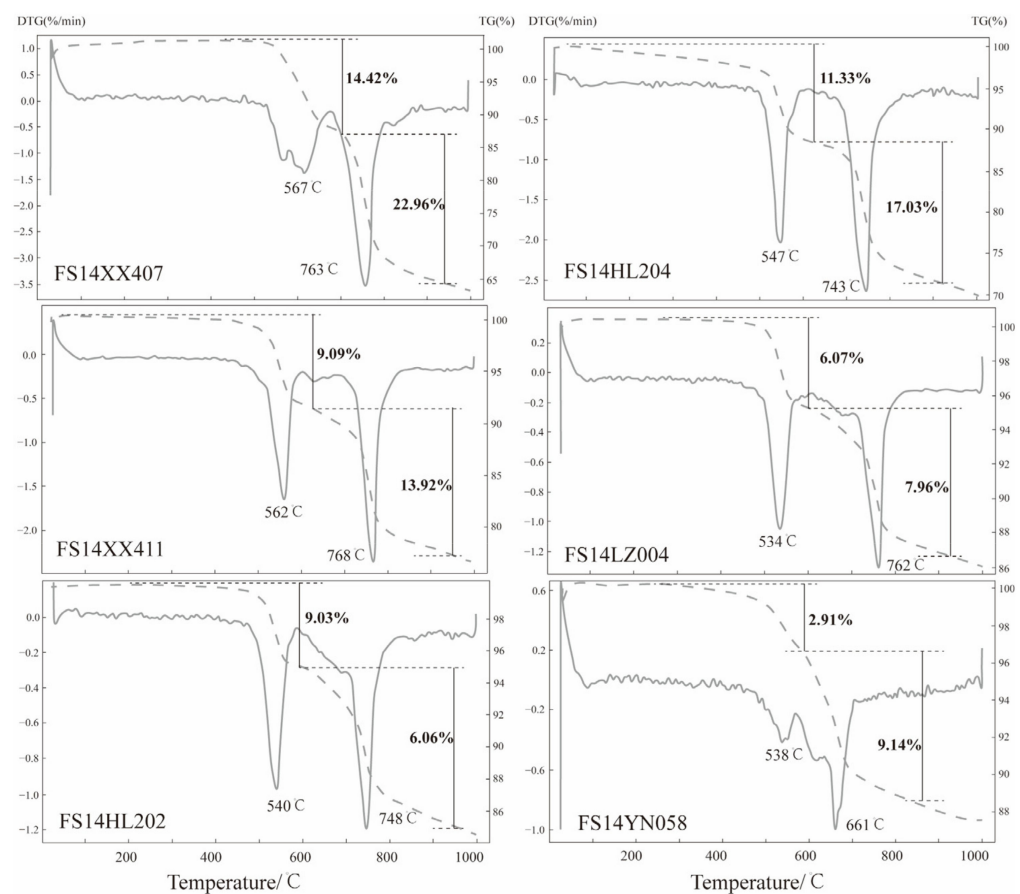


Figure 10. Differential thermal analysis curves of Fanshan alunite.

7. Discussion

7.1. Alunite Evolution Temperature

The crystallization habits of mineral crystals can fully reveal the integrity of crystal morphology under unrestricted conditions, which is significantly influenced by the physical and geochemical conditions during crystal growth [50]. There are significant differences in the particle size and crystalline shape of alunite among different stages in Fanshan (Figures 5 and 6). The larger euhedral or subhedral alunite crystals during the hydrothermal stage reflect favorable physical and geochemical conditions for mineral crystallization, indicating higher temperatures. On the other hand, the cryptocrystalline alunite during the supergene stage indicates rapid crystallization, occurring in a lower-temperature environment that is unfavorable for the formation of complete crystal forms.

Moreover, the formation temperature of alunite can be inferred not only from the degree of crystallization but also from the elemental composition. Stoffregen and Cygan [51] conducted experimental studies on the extent of K-Na substitution reactions in alunite, and they found a positive correlation between Na content and temperature: there is less Na substitution for K, resulting in a K/Na molar ratio of up to 9 at 250 °C and 500 bars; K-alunite and Na-alunite can form completely miscible solid melts, with a K/Na molar ratio of up to 2.3 at 350 °C and 500 bars. Generally, alunite at temperatures above 200 °C contains a higher amount of K, with a K/Na molar ratio greater than 3 [52]. Typically, high-temperature alunite has higher Na and Ca contents [52–55], and the presence of APS minerals indicates higher formation temperatures [53]. IA alunite in Fanshan contains APS mineral nuclei (Figure 5d,h), and from IA to IB and then to II alunite, the contents of Na₂O, CaO, and H₂O decrease, while the K₂O content increases (Figure 7), indicating that the formation temperature of alunite in Fanshan gradually decreases with hydrothermal evolution. The K/Na molar ratio in EPMA of alunite ranges from 1.71 to 28.27, with an average of 14.13; the K/Na molar ratio in EDS ranges from 0.61 to 64.43, with an average of 9.66, indicating that the formation temperature of alunite is higher than 200 °C, which is consistent with the temperature characteristics of high-sulfidation epithermal deposits. This further confirms the presence of a high-sulfidation hydrothermal system in Luzong basin. However, the total content of K₂O and Na₂O (6.02% to 10.63%) in alunite differs significantly from the theoretical alkali metal content (11.37%). This difference is due to the high water content in alunite (≥16.59%) and the presence of H₃O-alunite [H₃OAl₃(SO₄)₂(OH)₆], explaining the higher water content and lower total K₂O and Na₂O contents in Fanshan alunite.

7.2. Alunite Phase Indication

The absorption peak near 3480 cm⁻¹ in the FT-IR spectra of alunite is caused by the stretching vibration of the -OH group [49,56]. The absorption spectra around 1080 cm⁻¹ result from the superposition of alunite and quartz, and the peaks at 796 cm⁻¹ and 682 cm⁻¹ are characteristic absorption spectra of quartz [57], which are attributed to the symmetric stretching vibration of Si-O-Si bonds in quartz [56]. The presence of peaks in the range of 1200–1000 cm⁻¹ and 700–600 cm⁻¹ indicates the presence of SO₄²⁻ groups in the measured samples. At the positions that can represent the spectral characteristics of alunite, such as 3480 cm⁻¹, 1080 cm⁻¹, 1200–1000 cm⁻¹, and 700–600 cm⁻¹, the FT-IR spectra of Fanshan alunite samples all have these spectral peaks. The development of peaks at 796 cm⁻¹ and 682 cm⁻¹ in the samples from top to bottom in Figure 8 indicates an increasing amount of quartz crystals, suggesting an environment that is less favorable for the formation of alunite. Based on the FT-IR spectra of alunite, combined with the formation stages and mineralization relationships (Figure 4), mineral morphology and particle size (Figures 5 and 6), and the negative correlation between the peaks at 3480 cm⁻¹ and 1080 cm⁻¹ (Figure 9), we infer that larger peaks at 3480 cm⁻¹ and smaller peaks at 1080 cm⁻¹ represent purer alunite samples with better crystal forms and larger crystals. Such alunite samples are formed at higher temperatures and have a closer relationship with hydrothermal mineralization.

The DTA of alunite typically involves two decomposition mechanisms: dehydroxylation and desulfidation [58]. The exothermic reactions observed in Fanshan alunite at around 550 °C and 750 °C correspond to the dehydroxylation and desulfation processes, respectively (Figure 10). The thermogravimetric analysis data (TG) show that the weight loss after the first exothermic reaction in the hydrothermal alunite is approximately 6.07% to 14.42%, which is lower than the theoretical weight loss of alunite (13.05%). This is due to the impurities present in the tested samples, such as minerals like quartz, which do not contain structural water or adsorbed water. The gradual shallowing of the second endothermic peak and the slowing down of the weight loss curve slope from the hydrothermal IA alunite (FS14HL204, FS14XX411, FS14LZ004, FS14HL202) to IB alunite (FS14XX407) and then to the less favorable supergene II alunite (FS14YN058) indicate a gradual decrease

in the formation temperature of alunite [59]. The better the crystallization of alunite, the stronger and more pronounced the desulfation process. Therefore, the degree of exothermic peaks and the slope or extent of weight loss in the TG curve can be used to infer the formation environment of alunite, which in turn provides insights into its relationship with mineralization and the potential for prospecting in the area.

In summary, the value and correlation of 3480 cm^{-1} and 1080 cm^{-1} peaks in the FT-IR spectra of alunite, as well as the characteristics of the exothermic peaks and weight loss slope in DTA curve, can be used to judge the forming environment of alunite. Combined with its genesis of alunite, it is possible to assess its mineralization potential and use these phase characteristics to indicate the locations of fluid that are more favorable for hydrothermal mineralization.

7.3. Alunite Prospecting Indication

Alunite, as a representative mineral in lithocaps generally formed in porphyry–epithermal systems near the surface, can reflect different geological environments [60]. Rye et al. [3] classified alunite into four formation environments, and alunite from different environments has different implications for studying its mineralogical and geochemical characteristics, assessing mineralization potential, and indicating exploration directions. Magmatic–hydrothermal alunite is formed through the reaction of acidic fluids generated by the SO_2 disproportionation in the deep-seated magmatic differentiation with the surrounding rocks [5,61,62]. It is often associated with high-sulfidation metal minerals such as enargite and other Cu-As-Sb-S minerals, indicating good mineralization potential and serving as a useful indicator mineral for exploring high-sulfidation and porphyry deposits [63]. Magmatic-steam alunite forms in high-temperature, low-pressure environments near the surface, where magma rapidly oxidizes and releases SO_2 [5]. It can form lithocaps, and its mineralization potential depends on specific conditions. Steam-heated alunite is formed by atmospheric oxidation of H_2S -containing gas in the permeate zone above the water table, which is released from deep boiling fluids [5,61,62]. This environment may produce epithermal deposits. Supergene alunite forms as a result of the atmospheric oxidation of sulfides and exhibits features of secondary enrichment. Its deep-seated mineralization potential cannot be inferred.

Hydrothermal alunite plays an indicative role in deposit exploration [5], and studying the spectroscopic, mineralogical, and geochemical characteristics of hydrothermal alunite can help further indicate the mineralization center. In their study of the Lepanto high-sulfidation deposit in the Mankayan area, Philippines, Chang et al. [3] found that alunite SWIR exhibited a significant indication at the 1480 nm absorption peak position. This peak position is closely related to the formation temperature of alunite. Alunite closer to the intrusion or hydrothermal center showed higher absorption at 1480 nm, while alunite farther away from the intrusion or hydrothermal center exhibited lower absorption at 1480 nm. Therefore, the systematic variation in the 1480 nm absorption peak position in the short-wave infrared spectrum of alunite can be used to locate the center of the intrusion and the position of porphyry mineralization [3]. Furthermore, the geochemical characteristics of hydrothermal alunite also exhibit systematic variations relative to the position of the intrusion: near the center of the intrusion, alunite shows a decrease in Pb content and an increase in Sr, La, La/Pb, and Sr/Pb ratios, while the Pb/(Na + K) molar ratio gradually decreases.

In addition to the aforementioned characteristics of alunite, the FT-IR spectroscopy and DTA conducted in this study also provide indications of the formation environment, crystallinity, and exploration direction of alunite. These data can be used to guide deposit exploration. Alunite with a larger peak at 3480 cm^{-1} and a smaller peak at 1080 cm^{-1} in FT-IR spectrum indicates a higher formation temperature and a closer relationship with hydrothermal mineralization. A deeper exothermic valley at 750°C and a steeper weight loss slope in the alunite DTA curve indicate a better formation environment for alunite, a closer relationship with mineralization, and a greater mineralization potential.

8. Conclusions

- There are three types of alunite produced from the hydrothermal stage to the supergene stage in the Fanshan area of the Luzong basin early-stage hydrothermal alunite (IA alunite) formed during the metasomatic alteration, late-stage hydrothermal alunite (IB alunite), and supergene alunite (II alunite). As the evolution progresses, the formation temperatures of these three types of alunite gradually decrease.
- The alunite in the Fanshan area of the Luzong basin is K-alunite. The total content of K₂O and Na₂O in the alunite is relatively lower than in the theoretical composition of alunite, and it contains a significant amount of water. H₃O-alunite [H₃OAl₃(SO₄)₂(OH)₆] is present in Fanshan. The high K/Na molar ratio indicates that the formation temperature of the alunite is above 200 °C, which is consistent with the temperature characteristics of high-sulfidation deposits. This further confirms the presence of a high-sulfidation epithermal system in the Luzong basin.
- As a representative mineral in the shallow alteration system for exploring high-sulfidation or porphyry deposits, hydrothermal alunite exhibits indicative properties regarding the formation environment, SWIR characteristics, and geochemical features of hydrothermal mineralization centers. In addition to these aspects, the FT-IR spectroscopy and DTA described in this article also demonstrate their indicative role. The FT-IR spectroscopic features of alunite with larger peak values at 3480 cm⁻¹ and smaller peak values at 1080 cm⁻¹, as well as the DTA curve features of deeper exothermic valleys at 750 °C and steeper weight loss slopes, indicate a favorable formation environment for alunite and provide valuable indications for deposit exploration and assessments of mineralization potential.

Author Contributions: Conceptualization, X.L. (Xuanxuan Li), Q.X., X.L. (Xin Lin), S.L. and M.T.; methodology, X.L. (Xuanxuan Li), Q.X., X.L. (Xin Lin), S.L. and M.T.; software, X.L. (Xuanxuan Li), Q.X., X.L. (Xin Lin), S.L. and M.T.; validation, X.L. (Xuanxuan Li); formal analysis, X.L. (Xin Lin); investigation, X.L. (Xuanxuan Li) and Q.X.; resources, X.L. (Xuanxuan Li) and Q.X.; writing—original draft preparation, X.L. (Xuanxuan Li); writing—review and editing, X.L. (Xuanxuan Li) and Q.X.; funding acquisition, X.L. (Xuanxuan Li) and Q.X. All authors have read and agreed to the published version of the manuscript.

Funding: This research was funded by the National Natural Science Foundation of China, grant number 42102082, 42202074, and Anhui Polytechnic University Talen Introduction Research Fund Project, grant number 2020YQQ073.

Data Availability Statement: Data available in a publicly accessible repository.

Acknowledgments: Thanks for the constructive suggestions and comments from reviewers that greatly improved the quality of the paper.

Conflicts of Interest: The authors declare no conflicts of interest.

References

1. Sillitoe, R.H. Porphyry copper systems. *Econ. Geol.* **2010**, *105*, 3–41. [[CrossRef](#)]
2. Cooke, D.R.; Agnew, P.; Hollings, P.; Baker, M.; Chang, Z.S.; Wilkinson, J.J.; White, N.C.; Zhang, L.J.; Thompson, J.; Gemmill, J.B.; et al. Porphyry indicator minerals (PIMS) and porphyry vectoring and fertility tools (PVFTS)-indicators of mineralization styles and recorders of hypogene geochemical dispersion halos. In Proceedings of the Exploration 17: Sixth Decennial International Conference on Mineral Exploration, Toronto, ON, Canada, 27 October 2017; Tschirhart, V., Thomas, M.D., Eds.; pp. 457–470.
3. Chang, Z.S.; Hedenquist, J.W.; White, N.C.; Cooke, D.R.; Roach, M.; Deyell, C.L.; Garcia, J.; Gemmill, B.J.; McKnight, S.; Cuison, L. Exploration tools for linked porphyry and epithermal deposits: Example from the Mankayan intrusion-centered Cu-Au district, Luzon, Philippines. *Econ. Geol.* **2011**, *106*, 1365–1398. [[CrossRef](#)]
4. Li, X.X.; Zhou, T.F.; White, N.C.; Fan, Y.; Zhang, L.J.; Xie, J.; Liu, Y.N.; Xiao, X. Formation of the Fanshan lithocap and implications for exploration in the Luzong basin, Anhui Province, China. *Ore Geol. Rev.* **2020**, *118*, 103314. [[CrossRef](#)]
5. Rye, R.O.; Bethke, P.M.; Wasserman, M.D. The stable isotope geochemistry of acid sulfate alteration. *Econ. Geol.* **1992**, *87*, 225–262. [[CrossRef](#)]
6. Xuan, Z.Q. Resources and tapping of alunite in China. *Geol. Chem. Miner.* **1998**, *20*, 279–286, (In Chinese with English abstract).
7. Li, Z.M. Status of alunite resources in China. *Ind. Miner. Process.* **1999**, *8*, 35. (In Chinese)

8. Wang, X.L.; Ji, C.S.; Ren, H.B. A study of present situation of comprehensive utilization and development prospect of alunite in China. *China Min. Mag.* **2010**, *19*, 15–21, (In Chinese with English abstract).
9. Bureau of Geology and Mineral Exploration of Anhui Province 327 Geological Team. *Hefei: Summary Report of Geological Exploration in Dafanshan Mining Area of Lujiang Alum Mine, Anhui Province*, 1962. (In Chinese)
10. Zhou, T.F.; Fan, Y.; Yuan, F.; Lu, S.M.; Shang, S.G.; Cooke, D.; Meffre, S.; Zhao, G.C. Geochronology of the volcanic rocks in the Luzong Basin and its significance. *Sci. China (Ser. D)* **2008**, *38*, 1342–1353. (In Chinese)
11. Zhou, T.F.; Wang, B.; Fan, Y.; Yuan, F.; Zhang, L.J.; Zhong, G.X. Apatite-actinolite-magnetite deposit related to A-type granite in Luzong basin: Evidence from Makou iron deposit. *Acta Petrol. Sin.* **2012**, *28*, 3087–3098, (In Chinese with English abstract).
12. Fan, Y.; Zhou, T.F.; Yuan, F.; Tang, M.H.; Zhang, L.J.; Ma, L.; Xie, J. High sulfidation epithermal hydrothermal system in Lu-Zong volcanic basin: Evidence from geological characteristics and sulfur isotope data of Fanshan alunite deposit. *Acta Petrol. Sin.* **2010**, *26*, 3657–3666, (In Chinese with English abstract).
13. Zhang, L.J. Polymetallic Mineralization and Associated Magmatic and Volcanic Activity in the Luzong Basin, Anhui Province, Eastern China. Ph.D. Thesis, Hefei University of Technology, Hefei, China, June 2011; pp. 1–289, (In Chinese with English abstract).
14. Li, X.X.; Zhang, L.J.; Gao, C.S.; Xie, J.; White, N.C. Geological and geochemical characteristics of lithocap in the Lu-Zong Basin, Anhui, China. *Acta Petrol. Sin.* **2017**, *33*, 3545–3558, (In Chinese with English abstract).
15. Li, X.X.; Zhou, T.F.; Fan, Y.; Liu, Y.N.; Chen, J.; Zhang, L.J.; White, N.C.; Xie, J. Geochronology and geological significances of Fanshan lithocap in Luzong basin, Anhui Province. *Acta Petrol. Sin.* **2019**, *35*, 3782–3796, (In Chinese with English abstract).
16. Li, X.X.; Zhou, T.F.; White, N.C.; Fan, Y.; Chen, J.; Liu, Y.N. Genesis of Fanshan lithocap, Luzong volcanic basin, Anhui Province, China—indications from alunite and pyrite isotopes. *Ore Geol. Rev.* **2020**, *127*, 103802. [[CrossRef](#)]
17. Zhou, T.F.; Fan, Y.; Wang, S.W.; White, N.C. Metallogenic regularity and metallogenic model of the Middle Lower Yangtze River Valley Metallogenic Belt. *Acta Petrol. Sin.* **2017**, *33*, 3353–3372, (In Chinese with English abstract).
18. Chang, Y.F.; Liu, X.P.; Wu, Y.C. *The Copper-Iron Belt of the Lower and Middle Reaches of the Changjiang River*; Geological Publishing House: Beijing, China, 1991; pp. 1–312. (In Chinese)
19. Zhai, Y.S.; Yao, S.Z.; Ling, X.D. *Regularities of Metallogenesis for Copper (Gold) Deposits in the Middle and Lower Reaches of the Yangtze River Area*; Geological Publishing House: Beijing, China, 1992; pp. 1–120. (In Chinese)
20. Ren, Q.J.; Liu, X.S.; Xu, Z.W.; Hu, S.X.; Hu, W.X. *Mesozoic Volcanic Tectonic Depression and Its Mineralizing Process in Lujiang-Zoyang Area, Anhui Province*; Geological Publishing House: Beijing, China, 1991; pp. 1–206. (In Chinese)
21. Lu, S.M.; Li, J.S.; Tang, J.F. Preliminary study on metallogenic geological conditions and background of the concentrating area of volcanic rock ores around Luzong. In Proceedings of the East China Six Provinces One City Geoscience Science and Technology Forum, Hefei, China, 15–17 November 2007; pp. 116–119, (In Chinese with English abstract).
22. Zhou, T.F.; Fan, Y.; Yuan, F.; Song, C.Z.; Zhang, L.J.; Qian, C.C.; Lu, S.M.; David, R.C. Temporal spatial framework of magmatic intrusions in Luzong volcanic basin in East China and their constrain to mineralizations. *Acta Petrol. Sin.* **2010**, *26*, 2694–2714, (In Chinese with English abstract).
23. Bureau of Geology and Mineral Exploration of Anhui Province 327 Geological Team. *Hefei: Fanshan Town, Jangjunmiao 1:50000 Regional Geological Survey Report*, 1981. (In Chinese)
24. Bureau of Geology and Mineral Exploration of Anhui Province 327 Geological Team. *Hefei: Yijinqiao, Zongyang County, Tanggou Town 1:50000 Regional Geological Survey Report*, 1985. (In Chinese)
25. Bureau of Geology and Mineral Exploration of Anhui Province 327 Geological Team. *Hefei: Shengqiao, Huailinzui, Shijianbu, Lujiang County, Kaichengqiao 1:50000 Regional Geological Survey Report*, 1988. (In Chinese)
26. Bureau of Geology and Mineral Exploration of Anhui Province 327 Geological Team. *Hefei: Niubu, Zhoutan 1:50000 Regional Geological Report*, 1994; pp. 1–276. (In Chinese)
27. Zhou, T.F.; Song, M.Y.; Fan, Y.; Yuan, F.; Liu, J.; Wu, M.A.; Qian, C.C.; Lu, S.M. Chronology of the Bajiatan intrusion in the Luzong basin, Anhui, and its significance. *Acta Petrol. Sin.* **2007**, *23*, 2379–2386, (In Chinese with English abstract).
28. Fan, Y.; Zhou, T.F.; Yuan, F.; Qian, C.C.; Lu, S.M.; Cooke, D. LA-ICP-MS zircon U-Pb ages of the A-type granites in the Lu-Zong (Lujiang-Longyang) area and their geological significances. *Acta Petrol. Sin.* **2008**, *24*, 1715–1724, (In Chinese with English abstract).
29. Fan, Y.; Qiu, H.; Zhou, T.F.; Yuan, F.; Zhang, L.J. LA-ICP MS zircon U-Pb dating for the hidden intrusions in the Lu-Zong basin and its tectonic significance. *Acta Geol. Sin.* **2014**, *88*, 532–546, (In Chinese with English abstract).
30. Wang, B.; Zhou, T.F.; Fan, Y.; Chen, J.; Liu, Y.N.; Chen, Y. Breccia, hydrothermal alteration and structural geology of the Huangtun deposit in the Middle-Lower Yangtze Metallogenic Belt, Eastern China. *Ore Geol. Rev.* **2020**, *120*, 103414. [[CrossRef](#)]
31. Zhou, T.F.; Wu, M.A.; Fan, Y.; Duan, C.; Yuan, F.; Zhang, L.J.; Liu, J.; Qian, B.; Pirajno, F.; Cooke, D.R. Geological, geochemical characteristics and isotope systematics of the Longqiao iron deposit in the Lu-Zong volcano-sedimentary basin, Middle-Lower Yangtze (Changjiang) River Valley, Eastern China. *Ore Geol. Rev.* **2011**, *43*, 154–169.
32. Liu, Y.N.; Fan, Y.; Zhou, T.F.; Xiao, X.; White, N.C.; Thompson, J.; Hong, H.L.; Zhang, L.J. Geochemical characteristics of magnetite in Longqiao skarn iron deposit in the Middle-Lower Yangtze Metallogenic Belt, Eastern China. *Miner. Depos.* **2019**, *54*, 1229–1242. [[CrossRef](#)]
33. Fan, Y.; Liu, Y.N.; Zhou, T.F.; Zhang, L.J.; Yuan, F.; Wang, W.C. Geochronology of the Nihe deposit and in the Lu-Zong basin and its metallogenic significances. *Acta Petrol. Sin.* **2014**, *30*, 1369–1381, (In Chinese with English abstract).

34. Zhou, T.F.; Fan, Y.; Yuan, F.; Wu, M.A.; Zhao, W.G.; Qian, B.; Ma, L.; Wang, W.C.; Liu, Y.N.; White, N.C. The metallogenic model of Nihe iron deposit in Lu-Zong Basin and genetic relationship between gypsum-salt layer and deposit. *Acta Geol. Sin.* **2014**, *88*, 562–573, (In Chinese with English abstract).
35. Liu, Y.N.; Fan, Y.; Zhang, L.J. Precipitation mechanism, REE characteristics of anhydrite in Nihe deposit and its relation to mineralization. *Acta Petrol. Sin.* **2017**, *33*, 3531–3544, (In Chinese with English abstract).
36. Liu, Y.N.; Fan, Y.; Zhou, T.F.; Zhang, L.J.; White, N.C.; Hong, H.L.; Zhang, W. LA-ICP-MS titanite U-Pb dating and mineral chemistry of the Luohe magnetite-apatite (MA)-type deposit in the Lu-Zong volcanic basin, Eastern China. *Ore Geol. Rev.* **2018**, *92*, 284–296. [[CrossRef](#)]
37. Nie, L.Q.; Zhou, T.F.; Fan, Y.; Zhang, L.J.; Cooke, D.R.; White, N.C. Geology, geochemistry and genesis of the Makou magnetite-apatite deposit in the Luzong volcanic basin, middle-lower Yangtze river valley metallogenic belt, eastern China. *Ore Geol. Rev.* **2017**, *91*, 264–277. [[CrossRef](#)]
38. Zhang, L.J.; Zhou, T.F.; Fan, Y.; Yuan, F.; Ma, L.; Qian, B. Dating of copper mineralization in Jingbian deposit and its prospecting significance in Luzong basin, Anhui Province. *Acta Petrol. Sin.* **2010**, *26*, 2729–2738, (In Chinese with English abstract).
39. Zhou, T.F.; Yuan, F.; Yue, S.C.; Liu, X.D.; Zhang, X.; Fan, Y. Geochemistry and evolution of ore-forming fluids of the Yueshan Cu-Au skarn-and vein-type deposits, Anhui Province, South China. *Ore Geol. Rev.* **2007**, *31*, 279–303. [[CrossRef](#)]
40. Qian, B.; Yuan, F.; Zhou, T.F.; Fan, Y.; Zhang, L.J.; Ma, L. Geology and S isotope geochemistry of Yueshan Pb-Zn deposit in Luzong basin. *Miner. Depos.* **2010**, *29* (S1), 1–2. (In Chinese)
41. Zhang, S.; Wu, M.A.; Wang, J.; Li, X.D.; Zhao, W.G.; Wei, G.H. The mineralization related with the syenite in Luzong basin, Anhui Province. *Acta Geol. Sin.* **2014**, *88*, 519–531, (In Chinese with English abstract).
42. Bureau of Geology and Mineral Exploration of Anhui Province 327 Geological Team. *Hefei: Investigation and Evaluation of Au-Cu Polymetallic Deposits in the Northeast Margin of Luzong Volcanic Rock Basin, Anhui Province*, 2017. (In Chinese)
43. Wu, C.N.; Ren, Q.J.; Yuan, H.C.; Zhang, K.J. Studies of relation between volcanic structures and background contents of gold in the northeastern Lujiang-Zongyang basin, Anhui Province. *Miner. Resour. Geol.* **1994**, *8*, 108–113, (In Chinese with English abstract).
44. Pan, G.Q.; Dong, E.Y. Volcanic structures in the Lujiang-Zongyang volcanic area and their ore controlling effects. *Reg. Geol. China* **1983**, *5*, 31–37, (In Chinese with English abstract).
45. Chang, L.H.; Chen, M.Y.; Jin, W.; Li, S.C.; Yu, J.J. *Manual for the Identification of Thin Sections of Transparent Minerals*; Geological Publishing House: Beijing, China, 2006; pp. 1–236. (In Chinese)
46. Scott, K.M. Solid solution in, and classification of gossan-derived members of the alunite-jarosite family, Northwest Queensland, Australia. *Am. Mineral.* **1987**, *72*, 178–187.
47. Lager, G.A.; Swayze, G.A.; Loong, C.K.; Rotella, F.J.; Richardson, J.W.; Stoffregen, R.E. Neutron spectroscopic study of synthetic alunite and oxonium substituted alunite. *Can. Mineral.* **2001**, *39*, 1131–1138. [[CrossRef](#)]
48. Gaied, M.E.; Chaabani, F.; Gallala, W. Alunite characterization in the upper Eocene clay deposits of Central Tunisia: An implication to its genesis. *Carbonates Evaporites* **2015**, *30*, 347–356. [[CrossRef](#)]
49. Makreski, P.; Jovanovski, G.; Dimitrovska, S. Minerals from Macedonia: XIV. Identification of some sulfate minerals by vibrational (infrared and Raman) spectroscopy. *Vib. Spectrosc.* **2005**, *39*, 229–239. [[CrossRef](#)]
50. Zhong, W.Z.; Hua, S.K. Growth units of anion coordination polyhedral and crystal habits. *J. Chin. Ceram. Soc.* **1995**, *23*, 464–470, (In Chinese with English abstract).
51. Stoffregen, R.E.; Cygan, G.L. An experimental study of Na-K exchange between alunite and aqueous sulfate solutions. *Am. Mineral.* **1990**, *75*, 209–220.
52. Aoki, M.; Comsti, E.C.; Lazo, F.B.; Matsuhisa, Y. Advanced argillic alteration and geochemistry of alunite in an evolving hydrothermal system at Baguio, northern Luzon, Philippines. *Resour. Geol.* **1993**, *43*, 155–164.
53. Stoffregen, R.E.; Alpers, C.N. Woodhouseite and svanbergite in hydrothermal ore deposits: Products of apatite destruction during advanced argillic alteration. *Can. Mineral.* **1987**, *25*, 201–211.
54. Aoki, M. Mineralogical features and genesis of alunite solid solution in high temperature magmatic-hydrothermal systems. *J. Geol. Surv. Jpn.* **1991**, *277*, 31–32.
55. Arribas, A.; Cunningham, C.G.; Rytuba, J.J.; Rye, R.O.; Kelly, W.C.; Podwysoki, M.H.; Mckee, E.H.; Tosdal, R.M. Geology, geochronology, fluid inclusion, and stable-isotope geochemistry of the Rodalquilar Au alunite deposit, Spain. *Econ. Geol.* **1995**, *90*, 795–822. [[CrossRef](#)]
56. Lu, Q.; Wu, R.H. A mineralogical study of Changhua Tianhuang Chicken-Blood Stone. *Acta Petrol. Et Mineral.* **2010**, *29*, 56–61.
57. Dai, H.; Zhang, Q.; Jiang, X.P.; Wang, Z. Gemmological and mineralogical characteristics of chicken-blood stone of alunite and quartz “Di” from Changhua. *J. Gems Gemmol.* **2011**, *13*, 27–30, (In Chinese with English abstract).
58. Küçük, F.; Yildiz, K. The decomposition kinetics of mechanically activated alunite ore in air atmosphere by thermogravimetry. *Thermochim. Acta* **2006**, *448*, 107–110. [[CrossRef](#)]
59. Wang, C.Z.; Jue, H.H. Mineralogical characteristics of alunite from Zijinshan gold-copper deposit. *Acta Miner. Sin.* **2013**, *33*, 329–336, (In Chinese with English abstract).
60. Arancibia, G.; Matthews, S. SEM and EPMA studies of supergene and hypogene alunite as an aid to K-Ar and ⁴⁰Ar/³⁹Ar geochronology of epithermal mineral deposits. In Proceedings of the 10th Congreso Geológico Chileno, Concepción, Chile, 6–10 October 2003; p. 7.

61. Arribas, A. Characteristics of high-sulfidation epithermal deposits, and their relation to magmatic fluid. *Mineral. Assoc. Can. Short Course* **1995**, *23*, 419–454.
62. Ebert, S.W.; Rye, R.O. Secondary precious metal enrichment by steam-heated fluids in the Crofoot-Lewis hot spring gold-silver deposit and relation to paleoclimate. *Econ. Geol.* **1997**, *92*, 578–600. [[CrossRef](#)]
63. Hedenquist, J.W.; Arribas, A. Exploration implications of multiple formation environments of advanced argillic minerals. *Econ. Geol.* **2023**, *117*, 609–643. [[CrossRef](#)]

Disclaimer/Publisher’s Note: The statements, opinions and data contained in all publications are solely those of the individual author(s) and contributor(s) and not of MDPI and/or the editor(s). MDPI and/or the editor(s) disclaim responsibility for any injury to people or property resulting from any ideas, methods, instructions or products referred to in the content.